Orientation-resolved domain mapping in tetragonal SrTiO₃ using polarized Raman spectroscopy

Dodd J. Gray, Jr.,[1,*] Tyler A. Merz,[2] Yasuyuki Hikita,[3] Harold Y. Hwang,[2,3] and Hideo Mabuchi[1]

[1]*Ginzton Laboratory, Stanford University, Stanford, California 94305, USA*
[2]*Geballe Laboratory for Advanced Materials, Stanford University, Stanford, California 94305, USA*
[3]*Stanford Institute for Materials and Energy Sciences, SLAC National Accelerator Laboratory, Menlo Park, California 94025, USA*

We present microscopically resolved, polarized spectroscopy of Raman scattering collected from tetragonal SrTiO₃. The anisotropic response of first-order Raman peaks within a single tetragonal domain has been measured. From these data, we assign symmetries to the phonons seen in the first-order Raman spectrum which is normally complicated by uncontrolled domain structure. Using a translation stage, we map the local domain orientation of a 3-μm^3 crystal volume near the laser focus and compare it to wide-field polarized images. This technique can be performed with readily available instruments and is relevant to the study of a wide range of related materials, interfaces, and devices.

I. INTRODUCTION

The coupled structural and electronic properties of SrTiO₃ have been heavily studied for decades; interest in SrTiO₃ itself has been motivated in part by its incipient ferroelectricity [1,2] and resulting anomalously large dielectric response at low temperatures [3,4]. Furthermore, SrTiO₃ is widely used as a growth substrate for many transition-metal oxides (including high-temperature superconductors) and emergent low-dimensional electron systems at their interfaces [5,6]. However, aspects of the intrinsic properties remain open questions.

A cubic-to-tetragonal phase transition is seen at $T_{\text{cub}\rightarrow\text{tet}} \approx$ 105 K in SrTiO₃. Since the 1960s, it has been known that this phase transition involves the softening of an R point (Brillouin zone corner) optical phonon to zero frequency, reducing the point group from O_h to D_{4h}. The unit cell doubles in length along the tetragonal axis while simultaneously rotating by 45° and enlarging by a factor of $\sqrt{2}$ in each linear dimension in the basal plane. This phase transition is associated with alternating rotation of the corner-sharing oxygen octahedra around one of the three cubic crystal axes and elongation of that axis $a^0a^0a^0$ to $a^0a^0c^-$ in the Glazer notation [7]. We will refer the tetragonal phase as X, Y, or Z oriented, labeling which cubic axis elongates and becomes the principal axis in the tetragonal phase (see Fig. 1).

Raman spectroscopy has proven instrumental for studying phonon modes in the tetragonal phase of SrTiO₃, especially the soft modes associated with the cubic-to-tetragonal phase transition and the aborted classical ferroelectric phase transition near 30 K [4]. In the cubic phase, no phonon modes are Raman active and only a broad, multiphonon spectrum is observed. In the tetragonal phase, several sharp phonon resonances appear in the Raman spectrum.

In previous studies of Raman scattering in tetragonal SrTiO₃, samples with uncontrolled domain structure were studied with laser beams larger than usual domain sizes (often smaller than 5 μm in linear dimension [8–10]). This complicates the interpretation of the polarization dependence of the single-phonon Raman peaks and thus the symmetry assignments of the associated phonon modes. Here, we report microscopically resolved polarized Raman spectroscopy performed simultaneously with wide-field polarized imaging on undoped tetragonal SrTiO₃. The local domain structure was imaged with polarized light microscopy and polarized Raman signals were collected from monodomain crystal regions. We confirm and further characterize the anisotropic response of several first-order Raman peaks and demonstrate sensitivity to all possible local tetragonal domain orientations. By comparing experimental data with models, we make assignments of observed peaks to irreducible representations of the D_{4h} point group differing from those previously reported in the literature [11–15]. Finally, we demonstrate spatial mapping of a twinned tetragonal domain structure using microfocused Raman imaging, which reproduces the gross features of wide-field imaging, but also shows additional fine structure due to its higher resolution.

II. EXPERIMENT

The samples probed in this study were commerical, undoped, [100]-cut SrTiO₃ (Shinkosha Co.). We used wide-field polarized light microscopy to image the twinned domain pattern and ensure that the 532-nm wavelength Raman excitation laser was focused in a monodomain crystal region. By continuously rotating the electric field polarization direction of the excitation and Raman-scattered light (held parallel to each other) in the crystal plane, and measuring the strengths of scattering peaks in the Raman spectrum, we locally probed the symmetry of four Raman-active phonon modes. A schematic of the optical assembly used in this experiment is shown in Fig. 2.

A linearly polarized 532-nm laser source is formed by frequency doubling light from a Nd:yttrium-aluminium-garnet laser (YAG) at 1064 nm with a periodically poled LiNbO₃ crystal (PPLN). The 532-nm light is separated from the 1064-nm light with a dichroic mirror (DM1), spatially filtered and carried to the microscope by passage through a single-mode optical fiber (SMF1) and then spectrally filtered by two bounces off of volume Bragg grating filters (VBG1 and VBG2) before passing through a half-wave plate on a motorized
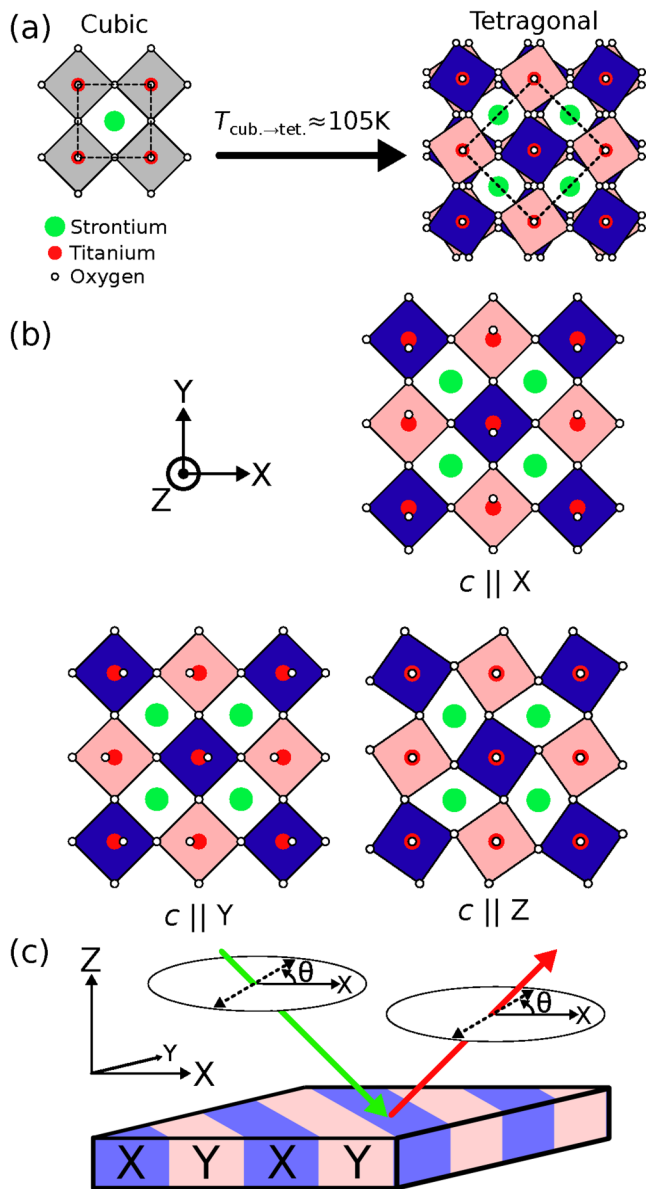
*dodd@stanford.edu

FIG. 1. (a) Two-dimensional representations of the cubic and tetragonal crystal structures formed by $SrTiO_3$. In the tetragonal phase, octahedra which rotate clockwise (counterclockwise) in the basal plane are shown as light pink (dark blue) squares. The black dashed lines in each crystal structure outline the unit cell. Two planes of oxygen octahedra are shown in the tetragonal structure, representing the doubling of the unit cell along the tetragonal principal axis. (b) Three possible orientations of the tetragonal principal c axis along the quasicubic crystal axes X, Y, and Z are possible. (c) Schematic drawing of the experimental geometry on a tetragonal STO sample with twinned X- and Y-oriented domains. Excitation laser light (light green arrow) is focused into the crystal and Raman-scattered light (red arrow) is collected. The polarizations of the excitation and Raman-scattered light are kept parallel and rotated within the X-Y plane of the crystal. Octahedral rotations are exaggerated for clarity.

rotation stage (HWP1) and alignment into the back aperture of a glass-corrected microscope objective (OBJ, Olympus LC PlanApo 60, NA = 0.7). The VBG filters serve to attenuate by 10^6 any collinear light more than 5 cm^{-1} (150 GHz)
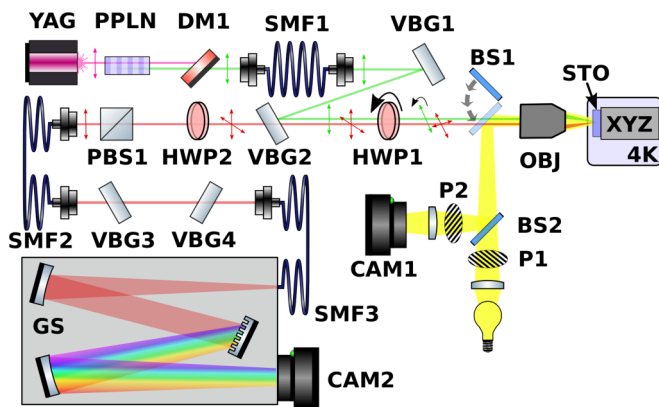

FIG. 2. Schematic of the polarized Raman microscope setup. Component labels are explained in the text.

above or below the laser frequency. This removes laser noise due to amplification as well as Raman and other nonlinear processes that are added in the light generation and fiber guiding processes.

Light collected by the objective makes a second pass through the motorized stage-mounted HWP1, thereby undoing the polarization rotation initially enacted on the input excitation light. It is in this way that rotating HWP1 serves to rotate the optical polarization relative to the fixed sample orientation (and thus crystal axes) without any change in the polarization of light elsewhere in the setup. VBG2 also serves as a dichroic beam splitter which separates the collected Raman light generated in the $SrTiO_3$ sample from elastically (Raleigh) scattered light recollected by the objective. After the isolated Raman scattered light transmits through VBG2, it passes through another half-wave plate (HWP2) and a polarizing beam splitter (PBS1) and is collected by an achromatic fiber couple based on an off-axis parabolic mirror. HWP2 is used to ensure that the polarization of the collected light is P such that it is transmitted through PBS1 while cross-polarized Raman light is rejected. Collecting Raman scattered light into another single-mode fiber (SMF2) spatially filters out residual Raleigh scattered light leaking through VBG2. The fiber-coupled Raman light is then coupled back into free space and passed through two more filters, VBG3 and VBG4. The series filtering of VBG2-4 attenuates recollected Raleigh scattered laser light by 10^9 while transmitting 67% of the Raman scattered light. Finally, the Raman signal is collected into a final single-mode fiber (SMF3) and sent into a homemade Czerny-Turner–type grating spectrometer (GS) with a diffraction limited resolution of 0.8 cm^{-1} (24 GHz) near 532 nm from which spectrographs are collected with a CCD camera (CAM2, Princeton Instruments Pixis 256). This setup allows for automated scanning of sample position and temperature, as well as optical polarization relative to the fixed crystal axes of a cryogenic sample. A removable pellicle beam splitter (BS1) between the rotating half-wave plate HWP1 and the microscope objective OBJ is used to couple in polarized wide-field illumination light and couple out the wide-field image. Another pellicle beam splitter (BS2) separates the illumination light from the wide-field image light, which is collected by a CMOS camera (Thorlabs DCC1545M).

Polarizers P1 and P2 serve as the polarizer and analyzer of this polarized imaging system, independently rotating of the linear polarization of the illumination and image relative to the fixed sample.

The spatial resolution of the measurement is set by the excitation laser spot size and depth of focus (Rayleigh length). The laser spot size at the surface has been measured to have an intensity full width at half-maximum of $\approx$300 nm. The depth of focus is estimated to be $\approx$600 nm in air ($n = 1$) for our excitation wavelength (532 nm) and objective numerical aperture (0.7). Accounting for the refractive index of SrTiO$_3$ ($n_{SrTiO_3} \approx 2.45$@532 nm [16]) suggests a depth of focus of $\sim$3 μm. Thus, we expect that the collected Raman signal acts as a probe of a material volume with $\sim$1 μm^2 transverse area and $\sim$3 μm depth. The SrTiO$_3$ sample is mounted on a stack of three piezo-stepper-type translation stages (Attocube) allowing three-dimensional positioning of the sample relative to the excitation laser focus.

The excitation laser powers used ranged from 25–45 mW and camera exposure times used to collect spectra ranged from 30 s to 2 min. The sample temperature was not measured with a thermometer, but was inferred from the collected spectral data as discussed in Sec. IV.

Relative to more common micro-Raman experiments on other materials (e.g., graphene), large excitation powers and long exposure times were necessary to measure Raman signals from SrTiO$_3$. This is mostly because the excitation photon energy (2.33 eV) is far below the 3.2-eV band-gap energy of SrTiO$_3$, dramatically reducing the Raman signal as compared

to that from materials with band gaps below 2.33 eV and thus a dense population of resonant interband dipole transitions.

The homemade grating spectrometer (GS) was originally roughly calibrated using a broadband laser source passed through a tunable filter and a commercial calibrated spectrometer (Thorlabs CCS175). While analyzing the data presented below, it became clear that the accuracy of this calibration was insufficient for inferring the sample temperature using measured spectra, as discussed in Sec. IV. To remedy this, we updated the calibration of collected spectra using the energies of two peaks in the Raman spectrum of tetragonal SrTiO$_3$, at 145 and 448 cm^{-1}. The energies of these peaks as well as the negligible temperature dependence of their energies in the 4–105 K temperature range are well established in the literature [11–15], making them suitable as references calibration. Our original calibrated dispersion (cm^{-1} per pixel) was adjusted by approximately 6% to meet the simultaneous requirements that complementary Stokes and anti-Stokes Raman peaks in our measured data were symmetric about the laser frequency and that our measured peaks close to 145 and 448 cm^{-1} matched those values.

III. ANALYSIS

Phonon modes of A_{1g}, B_{1g}, B_{2g}, and E_g symmetry are first-order Raman active in the tetragonal phase of SrTiO$_3$. We calculated the relative strength of the Raman response as a function of polarization angle θ, $I_{i,j}(\theta)$, for each possible mode symmetry i $\in \{A_{1g}, B_{1g}, B_{2g}, E_g\}$ and domain orientation

TABLE I. Anisotropic peak strengths for all Raman-allowed phonon symmetries and for all three possible domain orientations. Energies of observed peaks matching each symmetry are also given in the first column. Note that the peak energies associated with B_{2g} symmetry were used as calibration points for our spectra and thus these energies were not directly measured. Also note that the peak energies for A_{1g} and E_g correspond to the data presented in Fig. 3 and are temperature dependent. The energies measured for those peaks are within 0.8 cm^{-1} of the values in this table in all of the presented data.

| Symmetry	Raman Tensor	Case 1: $c \parallel X(\leftrightarrow)$		Case 2: $c \parallel Y(\updownarrow)$		Case 3: $c \parallel Z(\odot)$	
i	M_i	$M_{i,X}$	$I_{i,X}(\theta)$	$M_{i,Y}$	$I_{i,Y}(\theta)$	$M_{i,Z}$	$I_{i,Z}(\theta)$
A_{1g} (41.2 cm^{-1})	$\begin{bmatrix} a & 0 & 0 \\ 0 & a & 0 \\ 0 & 0 & b \end{bmatrix}$	$\begin{bmatrix} b & 0 \\ 0 & a \end{bmatrix}$	$\left(a\sin^2(\theta) + b\cos^2(\theta)\right)^2$	$\begin{bmatrix} a & 0 \\ 0 & b \end{bmatrix}$	$\left(a\cos^2(\theta) + b\sin^2(\theta)\right)^2$	$\begin{bmatrix} a & 0 \\ 0 & a \end{bmatrix}$	a^2
E_g (13.8 cm^{-1})	$\frac{1}{\sqrt{2}}\begin{bmatrix} 0 & 0 & e \\ 0 & 0 & e \\ e & e & 0 \end{bmatrix}$	$\begin{bmatrix} 0 & 0 \\ 0 & 0 \end{bmatrix}$	0	$\begin{bmatrix} 0 & e \\ e & 0 \end{bmatrix}$	$\frac{e^2}{2}\left(1 - \cos(4\theta)\right)$	$\begin{bmatrix} 0 & 0 \\ 0 & 0 \end{bmatrix}$	0
	$\frac{1}{\sqrt{2}}\begin{bmatrix} 0 & 0 & -e \\ 0 & 0 & e \\ -e & e & 0 \end{bmatrix}$	$\begin{bmatrix} 0 & -e \\ -e & 0 \end{bmatrix}$	$\frac{e^2}{2}\left(1 - \cos(4\theta)\right)$	$\begin{bmatrix} 0 & 0 \\ 0 & 0 \end{bmatrix}$	0	$\begin{bmatrix} 0 & 0 \\ 0 & 0 \end{bmatrix}$	0
B_{2g} (145 cm^{-1}, 448 cm^{-1})	$\begin{bmatrix} 0 & d & 0 \\ d & 0 & 0 \\ 0 & 0 & 0 \end{bmatrix}$	$\begin{bmatrix} 0 & 0 \\ 0 & d \end{bmatrix}$	$d^2\sin^4(\theta)$	$\begin{bmatrix} d & 0 \\ 0 & 0 \end{bmatrix}$	$d^2\cos^4(\theta)$	$\begin{bmatrix} -d & 0 \\ 0 & d \end{bmatrix}$	$d^2\cos^2(2\theta)$
B_{1g}	$\begin{bmatrix} c & 0 & 0 \\ 0 & -c & 0 \\ 0 & 0 & 0 \end{bmatrix}$	$\begin{bmatrix} 0 & 0 \\ 0 & 0 \end{bmatrix}$	0	$\begin{bmatrix} 0 & 0 \\ 0 & 0 \end{bmatrix}$	0	$\begin{bmatrix} 0 & c \\ c & 0 \end{bmatrix}$	$\frac{c^2}{2}\left(1 - \cos(4\theta)\right)$
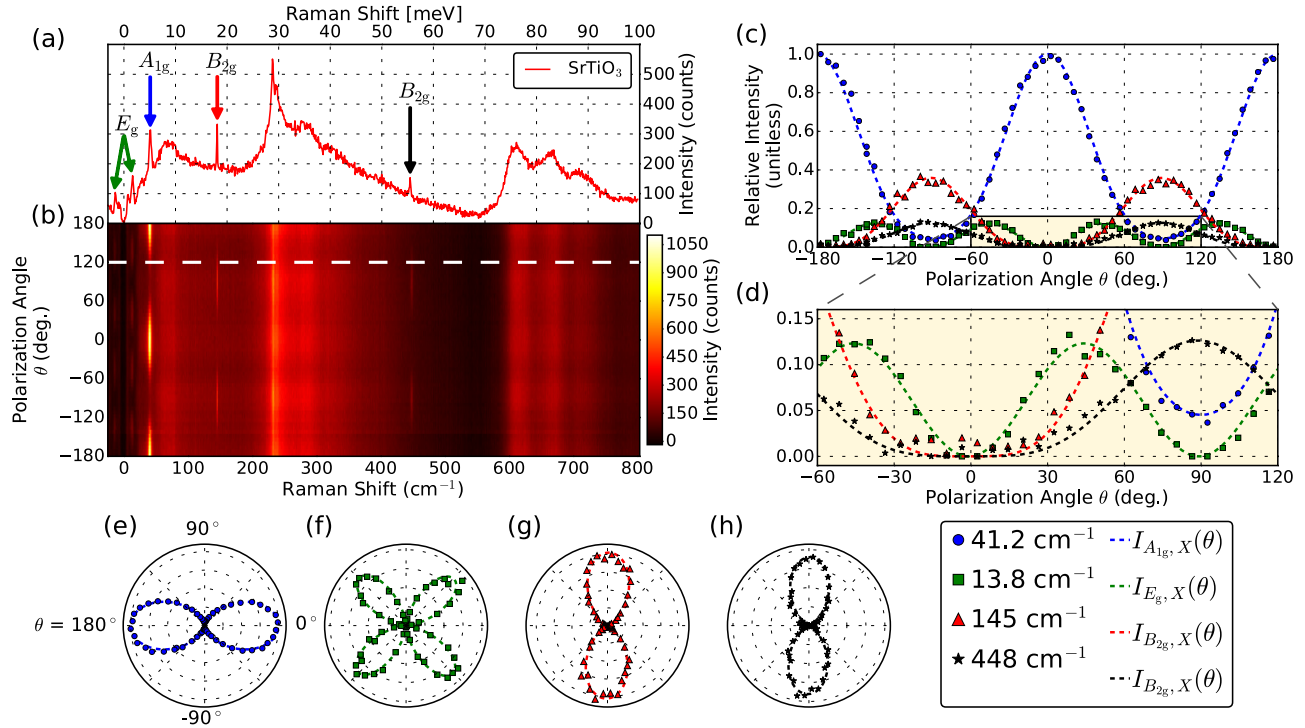
FIG. 3. (a) A typical Raman spectrum collected from an approximately 3-μm^3 volume of a tetragonal SrTiO$_3$ sample. As described in the text, the sample temperature at the laser focus is inferred from the spectrum to be between 50 and 60 K. The volume probed was approximately 100 μm below the surface. This spectrum was collected at polarization angle $\theta \approx 120°$, indicated by the white dashed line in (b). This angle was chosen for this plot because all of the relevant first-order Raman peaks are visible. (b) Polarization dependence of the Raman spectrum in (a) showing anisotropic strengths of first-order peaks. Comparison of these anisotropic responses with the three possibilities shown in Table I indicates that the tetragonal principal axis is along the X axis. The second E_g peak appearing to the left of 0 is the anti-Stokes shift complement of the peak appearing just to its right. (c) Measured polarization variation of the four peaks labeled in (a) and fits to anisotropic scattering intensities $I_{i,X}(\theta)$ given in Table I. (d) Zoomed-in view of the highlighted region in (c) showing that that a nonzero signal is measured from the A_{1g} peak (blue circles) at $\theta = 90°$. (e)–(h) Normalized polar plots of the same data shown in (c) for comparison with Table I. The legend at the bottom right applied to subplots (c)–(h).

$j \in \{X, Y, Z\}$. The details of this analysis are given in Appendix B. A summary of the results are given in Table I along with diagrams showing the form of $I_{i,j}(\theta)$ expected for each combination of crystal orientation and phonon symmetry.

Examining Table I, we see that the anisotropic Raman response of the A_{1g} peak has twofold rotational symmetry when the principal axis is aligned along one of the in-plane quasicubic axes (X or Y) and that the expected $I_{i,j}(\theta)$ patterns in these two cases are 90° rotated with respect to one another. There is some ambiguity in the direction of the larger nodes, characterized by the ratio of a to b in the A_{1g} pattern seen in Table I; as will be explained later in more detail, we have chosen $b > a$ for these figures to match the experimentally seen case of SrTiO$_3$. In contrast, we find either fourfold or continuously rotationally symmetric functions $I_{i,Z}(\theta)$ when the principal axis is out of plane (along Z). These differences allow for unambiguous assignment of local tetragonal axis orientation in a multidomain sample. As will be shown below, this can be accomplished in the present case using only the polarization dependence of the A_{1g} peak strength.

IV. RESULTS AND DISCUSSION

A typical polarized Raman spectrum collected from tetragonal SrTiO$_3$ with our setup is shown in Fig. 3(a).

Four labeled peaks from first-order (single-phonon) Raman scattering processes appear above the broad, second-order Raman background. The variation of the spectrum at one position in the sample with in-plane polarization angle θ is plotted in Fig. 3(b). The intensities of the labeled peaks can be seen varying with polarization against an almost constant background. The tetragonal principal axis of the probed crystal volume is determined to be along the X axis by comparison with the anisotropic responses predicted in Table I. Peak frequencies and strengths were analyzed by fitting Gaussian line shapes to the measured spectra in the vicinity of the peaks.

The X and Y laboratory coordinate axes were chosen to be along the high-symmetry axes of the measured $I_{A_{1g}}(\theta)$ polarization dependence. From the analysis discussed in Sec. III we infer that these directions correspond to the quasicubic axes of the tetragonal SrTiO$_3$ sample. When more than one position in the sample was probed (as will be shown in Figs. 4 and 5), the X and Y axes determined using data from the first position probed were used to analyze data from all subsequent positions.

The temperature of the sample at the laser focus was inferred from the measured spectral data in two ways. First, we considered the ratio of the Gaussian line-shape amplitudes fit to the Stokes and anti-Stokes E_g peaks. For the data presented in Fig. 3, the energy of this peak is 13.8 cm^{-1} and the
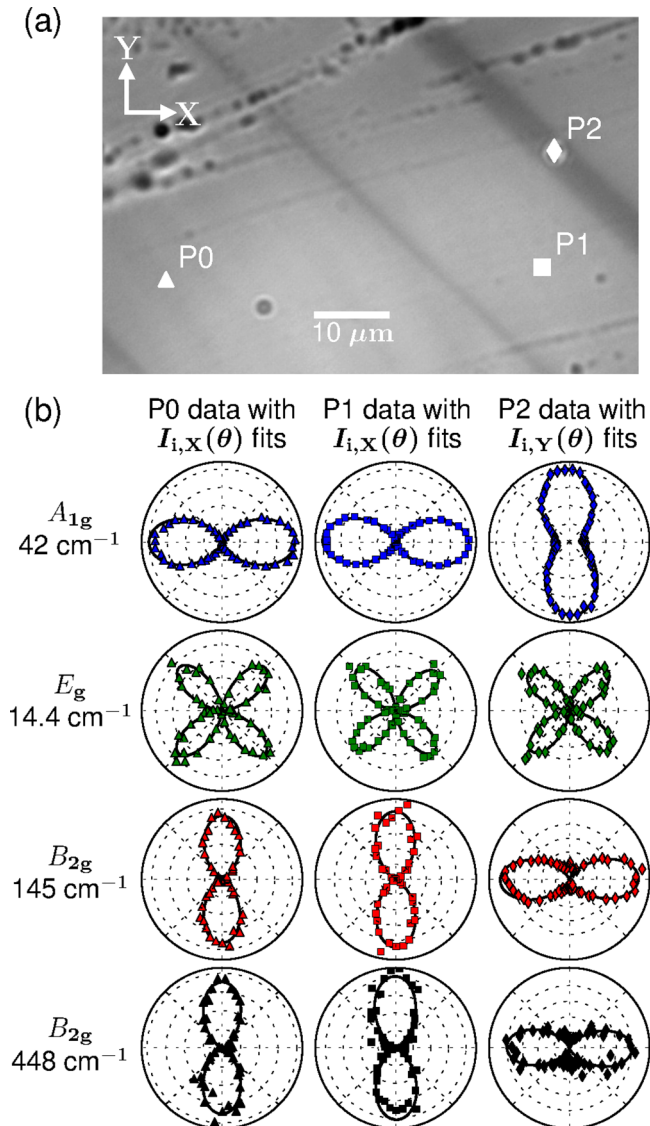
(a)

(b)

| | P0 data with $I_{i,X}(\theta)$ fits | P1 data with $I_{i,X}(\theta)$ fits | P2 data with $I_{i,Y}(\theta)$ fits |

A_{1g}
42 cm^{-1}

E_{g}
14.4 cm^{-1}

B_{2g}
145 cm^{-1}

B_{2g}
448 cm^{-1}

FIG. 4. (a) Tetragonal SrTiO$_3$ viewed in a wide-field microscope image. Polarization-dependent Raman spectra were collected approximately 100 μm below the surface at the three labeled points. (b) Polarization dependence of first-order Raman peaks at points P0, P1, and P2 indicated in (a). The analysis and data processing used to produce these plots are identical to that used for Figs. 3(c)–3(f). Comparison of the data with the anisotropic Raman intensities calculated in Table I indicates that lighter areas in the wide-field image (P0 and P1) are X-oriented tetragonal domains while darker areas (P2) are Y-oriented tetragonal domains. Spectral temperature signatures (described in the text) suggest the sample temperature at the laser focus was between 45 and 55 K.

Stokes/anti-Stokes ratio was found to be 1.46 $\pm$ 0.18. The temperature dependence of this ratio is known [17] to be

$$\frac{I_{\text{Stokes}}}{I_{\text{anti-Stokes}}} = e^{\frac{h\nu}{k_{\text{B}}T}}. \qquad (1)$$

From this, we infer that the sample temperature at the laser focus was 52.9 K although the measurement error of $\pm$0.18 in the $I_{\text{Stokes}}/I_{\text{anti-Stokes}}$ ratio leads to large error bars on this temperature measurement, giving 40.5 K $<T<$ 80.9 K. Next, the temperatures associated with the measured energies
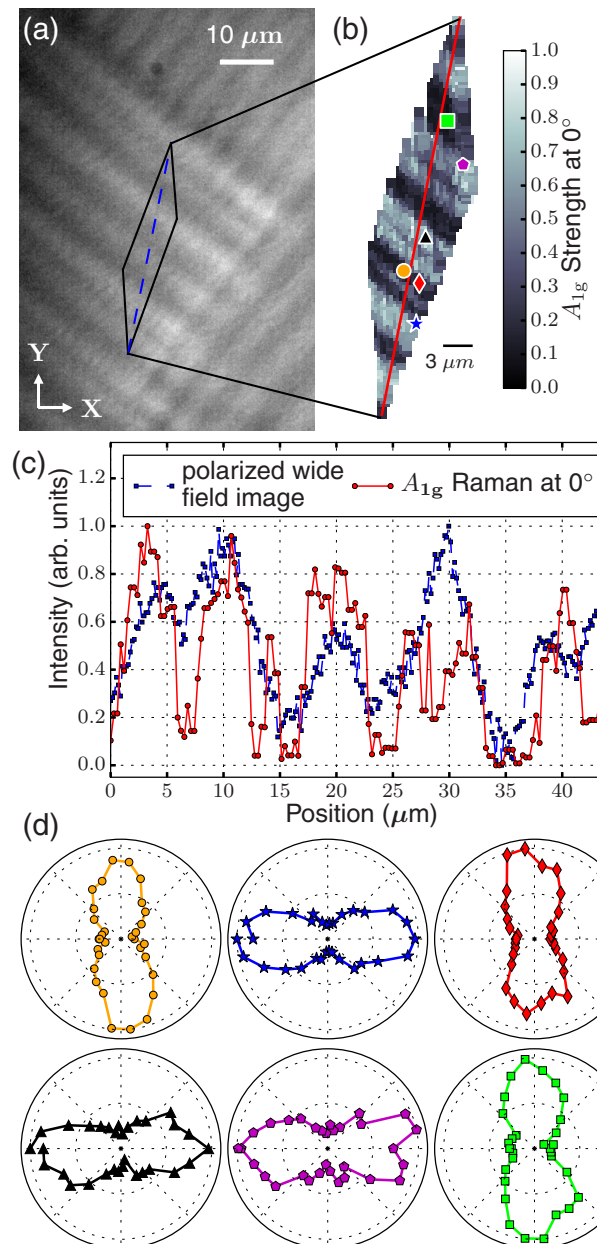

FIG. 5. (a) Wide-field, polarized microscope image of tetragonal SrTiO$_3$ showing dense twinning of X- and Y-oriented tetragonal domains with walls running at approximately 45° with respect to the in-plane quasicubic axes. A scanning-confocal measurement of the Raman signal for excitation light polarized along the X axis (0° in polar plots) was performed at a depth near 100 μm in the approximately parallelogram-shaped region outlined in black. The dashed blue line running diagonally through the parallelogram indicates the line cut of wide-field image intensity plotted in (c). (b) Relative strength of the A_{1g} Raman peak measured at points spaced by $\sim$1 μm in the region outlined in (a). Stripes of varied intensity are seen in a similar pattern to that observed from this region in the wide-field image. Light and dark regions are interpreted to be X- and Y-oriented tetragonal domains, respectively. The red line indicates a line cut in the of the mapped intensity plotted in (c). (d) Polar plots of A_{1g} strength measured at the points indicated with matching symbols in (b). As in Fig. 4, spectral temperature signatures (described in the text) suggest the sample temperature at the laser focus was between 45 and 55 K.

of the E_g (13.8 cm^{-1}) and A_{1g} (41.2 cm^{-1}) peaks were interpolated using the established temperature dependencies of these phonon energies [12]. Using this method, we inferred temperatures of 59.2 and 49.9 K from the E_g and A_{1g} energies, respectively. The agreement between these independent spectroscopic temperature signatures leads us believe that the temperature of the probed sample volume was in the 50–60 K range for the data presented in Fig. 3. The same analysis performed on the data presented in Figs. 4 and 5 suggests the sample temperature at the laser focus was in the 45–60 K range for all of the experiments presented in this study. Since this temperature range is well below $T_{\text{cub} \to \text{tet}} \approx 105$, we assume the SrTiO$_3$ crystal to be in the tetragonal phase with D_{4h} symmetry in all further discussion.

Raman spectra collected using a variety of scattering geometries have been used to assign irreducible representations of D_{4h} to phonons associated with first-order (sharp) peaks observed in tetragonal SrTiO$_3$ [12,13,15,18]. In particular, it is well established that the sharp peaks which appear near zero frequency below 105 K and harden to nearly 15 and 48 cm^{-1} at 4 K are E_g and A_{1g} phonon modes, respectively. As seen in Table I and Figs. 3(e) and 3(f), our data and analysis are consistent with this assignment, provided [15] that $b > a$ in the Raman tensor; we are able to make this assignment because of the relative orientation of the stronger A_{1g} lobes to the lobes of the B_{2g} modes which are uniquely defined by only one number. We differ from previous studies in our interpretation of the peaks seen at 145 and 448 cm^{-1}. Some authors have assigned both of these modes to nearly degenerate B_{1g} and E_g phonons [12,13] and others to nearly degenerate B_{2g} and E_g phonons [15,18]. Our experimental data and calculations of $I_{i,B_{1g}}(\theta)$ and $I_{i,B_{2g}}(\theta)$ are consistent with both of these modes corresponding only to B_{2g}. This is further corroborated by modal analysis (performed using the SAM package of Bilbao Crystallographic) [19–22] of the space group of tetragonal SrTiO$_3$ (D_{4h}^{18}, Wyckoff positions $4a$, $4b$, $4c$, and $8h$).

The Γ-point phonon modes are decomposed as

$$\Gamma = 1A_{1g} + 1A_{1u} + 2A_{2g} + 4A_{2u} + 1B_{1g}$$
$$+ 1B_{1u} + 2B_{2g} + 6E_u + 3E_g. \tag{2}$$

This decomposition suggests that one A_{1g} mode, one B_{1g} mode, two B_{2g} modes, and three E_g modes are allowed by symmetry to be active in first-order Raman scattering [18,23–25]. Our assignments of irreducible representations to observed modes are consistent with this decomposition, although only one E_g mode is identified in our data and no B_{1g} mode is identified. In contrast, assignment of both the 145- and 448-cm^{-1} peaks to B_{1g} violates this decomposition. This discrepancy seems rooted in whether the true crystal axes or the quasicubic axes in the basal plane of the tetragonal structure are used in the symmetry analysis [12,13,15] since the 45° rotation needed to transform between them interchanges the form of the B_{1g} and B_{2g} representations. We note that symmetry allows two more E_g than are observed in our data. We believe that their tensor elements are too small to observe in the present experiments. A single Raman-active B_{1g} mode is also allowed by symmetry, but we do not expect to see any evidence of this mode in the present data since it is not allowed by selection rules in either of the observed in-plane domain orientations.

We would like to highlight the strong anisotropy observed in the Raman response of the A_{1g} phonon mode seen near 41 cm^{-1} in our experiments. This anisotropy was noted by Gibhardt *et al.* [15], however, to our knowledge its microscopic origin is not known. As emphasized in Figs. 3(c) and 3(d), weak but finite signal was observed at the minima of the A_{1g} polarization dependence, allowing us to infer the ratio of Raman tensor elements a and b in Table I. The fit of $I_{A_{1g},X}(\theta)$ to the data shown in Fig. 3(c) suggests the Raman tensor coefficient ratio $b/a \approx 4.69 \pm 0.14$. This anisotropy seems large compared to the relatively minor anisotropy in the electron band structure caused by the cubic-to-tetragonal phase transition at $T_{\text{cub} \to \text{tet}}$. The comparatively minor anisotropy in refractive index [26] $\Delta n/n \approx 2 \times 10^{-5}$ suggests that the interband dipole coupling perturbed in the Raman scattering process is not itself significantly anisotropic. We believe this suggests that anisotropy (due to the tetragonal splitting) in the joint density of states between Ti$_{3d}$ conduction bands near this phonon energy (≈ 5.1 meV near 50 K) is the cause of the large observed A_{1g} Raman anisotropy, but further study, especially theoretical, is needed.

We note that in our data the peaked signal near 232 cm^{-1} does show twofold rotationally symmetric anisotropy of $\sim 15\%$ and that another weaker, broader twofold anisotropy appears 180° out of phase near 238 cm^{-1}. The broad background in this spectral region is present in Raman data from the cubic phase of SrTiO$_3$ above $T_{\text{cub} \to \text{tet}}$ and is attributed to multiphonon processes [11,12,27]. This broad background also displays fourfold rotationally symmetric variation. The sharper, twofold symmetric features are not strong enough relative to that background for the curve-fitting analysis performed on the other four peaks. The peak near 232 cm^{-1} has tentatively been assigned to B_{1g} [15,18] and B_{2g} [13,23] in previous literature, although the suggestion has also been made that it could result from multiphonon processes [12,15]. The symmetry and phase of the anisotropy observed in our data would be consistent with B_{2g} symmetry. Considering the proximity of these features to known multiphonon resonances seen above $T_{\text{cub} \to \text{tet}}$ together with our analysis of the four stronger peaks discussed above, we do not believe that the evidence supports either of these features resulting from single-phonon Raman processes.

Having established the polarization dependence of Raman scattering within a single domain, we now turn to investigating the domain structure seen in polarized light microscopy *via* micro-Raman mapping. A wide-field, polarized microscope image of twinned SrTiO$_3$ is shown in Fig. 4(a). Polar plots of Raman peaks similar to those in Figs. 3(e)–3(h) collected from material roughly 100 μm below the surface at the three points labeled in Fig. 4(a) are shown in Fig. 4(b). The anisotropic intensity patterns from point P2 are 90° rotated with respect to those collected from points P0 and P1. Comparing the anisotropic Raman signals measured at these three points with the first two columns of Table I, we infer that the dark regions in the polarized wide-field image correspond to Y-oriented domains, while the light regions correspond to X-oriented domains (cases 2 and 1 in Table I, respectively). These domain assignments are consistent with the observed 45° orientation of the domain walls with respect to the in-plane quasicubic crystal axes [28]. We note that while identical experiments were performed with more than 10 similar samples, evidence

of tetragonal domains with principal axes aligned out of plane (Z domains, case 3 in Table I) were only observed within approximately 10–20 μm of the sample edges and none of the observed Z domains were wide enough ($>3\,\mu$m) to allow for collection of Raman signal from a sample volume entirely contained within one domain [29]. We suspect this bias for in-plane tetragonal domain orientation at low-temperature results from built-in strains in the samples, possibly resulting from the polishing process [30].

Three features of the data presented in Fig. 4 are of note. First, the fitted $I_{i,j}(\theta)$ show some minor tilting ($<3°$ in all cases) with respect to the X and Y axes. Tilts measured from the fits of the different peaks at the same point are not well correlated and thus we believe these small tilts result from fitting to noisy data and are insignificant. Second, these data suggest that the contrast seen in polarized microscope images of twinned tetragonal $SrTiO_3$ are in fact domains and not domain walls. This is relevant to the results presented by Kalisky *et al.* [31] and Noad *et al.* [32] with similar features seen in maps of near-surface current density and superconductivity. Finally, we note that the ratio of A_{1g} tensor coefficients b/a inferred from the fits of $I_{A_{1g},X}(\theta)$ to the data from points P0 and P1 (5.8 ± 0.4 and 6.7 ± 0.3, respectively) is comparable to the value 4.7 ± 0.1 found by analyzing the data shown in Fig. 3(c), while the ratio 2.7 ± 0.1 found by fitting $I_{A_{1g},Y}(\theta)$ to the data from P2 is substantially smaller. This is not caused by a weak signal. The maximum strength of the A_{1g} signal at point P2, seen near $\theta = 90°$, was approximately 75% the maximum strength observed at points P0 and P1 near $\theta = 0°$. In fact, the A_{1g} signal strength was above the noise floor of the measurement for all polarization angles θ at all three points. It is possible that leakage of Raman scattering from adjacent domains into the collected signal could cause this. In that case, we would expect stronger signatures of such leakage in the polarization dependencies the B_{2g} peaks in Fig 4. Also, as will be shown in Fig. 5 below, the spatial resolution of the measurement appears to be sufficient to probe a region contained entirely within the approximately 5-μm-wide domain containing P2. A third possibility is that the b/a ratio in the A_{1g} Raman tensor is modulated by strain generated by the domain structure itself. This is left as a topic for future investigation.

Figure 5(a) shows a wide-field polarized microscope image of a densely twinned sample region. Domain walls appear at 45° with respect to the in-plane quasicubic axes, suggesting alternating X- and Y-oriented domains. Spectra were collected from points in the area outlined in Fig. 5(a). For the majority of spatial points, only one polarization angle (along X) was probed. Full polarization scans were also performed at a few randomly selected points. A map of the A_{1g} strength measured along X in the area outlined in Fig. 5(a) is shown in Fig. 5(b). Corresponding line cuts were taken from the polarized wide-field image [dashed blue line in Fig. 5(a)] and the scanning micro-Raman data [red line in Fig. 5(b)]. They are plotted together for comparison in Fig. 5(c). Similar features are seen in both line cuts, however, we note that some thin domains appear in the scanning Raman data that do not appear in the wide-field image data. We believe these differences are caused by an offset between the focal plane of the wide-field image which was taken with the focal plane near the surface and the focal plane scanning confocal Raman

image (focused approximately 100 μm below the surface). The thinner domains seen in the scanning image are likely pinched off below the surface of the material. We also see in Fig. 5(c) that scanning Raman offers much higher spatial resolution of domain-wall features ($\approx 1\,\mu$m as expected from the laser spot size) than wide-field imaging. The sharpness of the domain walls shown here lowers the upper bound on tetragonal $SrTiO_3$ domain-wall width of 5 μm given by Merz *et al.* [29].

Locations where full polarization scans were performed are indicated in Fig. 5(b) with different markers. Plots of the anisotropic A_{1g} response measured at each point indicated in Fig. 5(b) are shown in Fig. 5(d). Spectral data were collected for 20 s at each position forming the confocal image at at each polarization at the marked positions where polarization scans were performed. The data shown in Fig. 5(d) are much noisier than similar plots shown in Fig. 4, where a collection time of 2 min was used for data point. Nonetheless, the local tetragonal domain orientation is still clearly discernible in each case. We see that shapes of local A_{1g} responses in Fig. 5(d) correlate as expected with the color of the region in Fig. 5(b) where each anisotropic response was measured.

V. CONCLUSIONS

We have performed polarized Raman spectroscopy on tetragonal $SrTiO_3$ with microscopic spatial resolution and continuous polarization variation. Microscopic spatial resolution has allowed us to identify the local tetragonal domain orientation with a Raman signal and to study the anisotropic responses of first-order Raman peaks within a single tetragonal domain. The rotational symmetries of the measured anisotropic Raman signals have allowed us to assign them to irreducible representations of the D_{4h} point group with higher confidence than previously achieved in experiments sampling from many tetragonal domain orientations in multidomain samples. Our data and analysis suggest that the Raman peaks at 145 and 448 cm^{-1} both correspond only to phonons of B_{2g} symmetry, in contrast with previous reports.

We stress that the confocal polarized Raman imaging technique demonstrated in this paper can be performed with standard micro-Raman spectroscopy equipment. In fact based on the higher efficiency and lower amplifier noise of modern back-illuminated CCD cameras relative to the CCD used in our custom-built setup, we expect that the same signal-to-noise ratio as seen in the data presented here could be readily achieved with a 5–10× reduction in spectrum collection time. This technique allows mapping of local crystal structure and orientation in three dimensions with a resolution near the optical diffraction limit. We expect that it should be generally applicable to a wide variety of materials, interfaces, and devices in which domains or other spatially inhomogeneous structures are present.

APPENDIX: ANISOTROPIC RAMAN RESPONSE CALCULATION

The tensors describing the polarization-dependent response of these Raman-allowed phonon symmetries are given by their irreducible representations M_i. We calculate the expected polarization-dependent Raman intensity for each mode symmetry $I_i(\theta)$ by first rotating the basis of M_i by $45°$ around the tetragonal principal axis to match the quasicubic crystal axes:

$$M_{i,qc} = R_{3,45°}^{-1} M_i R_{3,45°}, \quad i \in \{A_{1g}, B_{1g}, B_{2g}, E_g\} \quad \text{(A1)}$$

where here the subscript 3 refers to the tetragonal principal axis and $R_{3,45°}$ represents a $45°$ rotation around that axis. We choose to work in the basis of the two-dimensional E_g space corresponding to oxygen tetrahedra rotations about the nonprincipal quasicubic crystal axes as this matches the symmetry of our experimental configuration and simplifies the math.

We find the 2×2 matrices describing polarization dependence of $\bar{Z}(XX)Z$ Raman scattering from tetragonal SrTiO$_3$ with its principal axis oriented along axis j, $M_{i,j,qc}(\theta)$, $j \in \{X, Y, Z\}$, by rearranging the indices to match the crystal orientation and deleting the third row and column corresponding to Z since no polarization should be excited or detected along this direction. Finally, we represent the action of polarizing the input and output light and rotating the polarization relative to the crystal axes in the X-Y plane with cascaded projection (P_j) and rotation ($R_{j,\theta}$) matrices and square the final tensor element to find $I_{i,j}(\theta)$:

$$I_{i,j}(\theta) = \left[P_X R_{Z,\theta}^{-1} M_{i,j,qc} R_{Z,\theta} \begin{bmatrix} 1 \\ 0 \end{bmatrix} \right]^2,$$
$$i \in \{A_{1g}, B_{1g}, B_{2g}, E_g\}, \quad j \in \{X, Y, Z\} \quad \text{(A2)}$$

where the $\begin{bmatrix} 1 \\ 0 \end{bmatrix}$ above corresponds to input light polarization along X.

[1] K. A. Müller and H. Burkard, Phys. Rev. B **19**, 3593 (1979).

[2] S. E. Rowley, L. J. Spalek, R. P. Smith, M. P. M. Dean, M. Itoh, J. F. Scott, G. G. Lonzarich, and S. S. Saxena, Nat. Phys. **10**, 367 (2014).

[3] G. A. Samara, Phys. Rev. **151**, 378 (1966).

[4] M. A. Saifi and L. E. Cross, Phys. Rev. B **2**, 677 (1970).

[5] H. Y. Hwang, Y. Iwasa, M. Kawasaki, B. Keimer, N. Nagaosa, and Y. Tokura, Nat. Mater. **11**, 103 (2012).

[6] P. Zubko, S. Gariglio, M. Gabay, P. Ghosez, and J.-M. Triscone, Annu. Rev. Condens. Matter Phys. **2**, 141 (2011).

[7] A. M. Glazer, Acta Crystallogr., Sect. B **28**, 3384 (1972).

[8] T. S. Chang, Appl. Phys. Lett. **17**, 254 (1970).

[9] M. Honig, J. A. Sulpizio, J. Drori, A. Joshua, E. Zeldov, and S. Ilani, Nat. Mater. **12**, 1112 (2013).

[10] B. Kalisky, E. M. Spanton, H. Noad, J. R. Kirtley, K. C. Nowack, C. Bell, H. K. Sato, M. Hosoda, Y. Xie, Y. Hikita, C. Woltmann, G. Pfanzelt, R. Jany, C. Richter, H. Y. Hwang, J. Mannhart, and K. A. Moler, Nat. Mater. **12**, 1091 (2013).

[11] C. H. Perry, J. Chem. Phys. **47**, 1619 (1967).

[12] P. A. Fleury, J. F. Scott, and J. M. Worlock, Phys. Rev. Lett. **21**, 16 (1968).

[13] J. Petzelt, T. Ostapchuk, I. Gregora, I. Rychetský, S. Hoffmann-Eifert, A. V. Pronin, Y. Yuzyuk, B. P. Gorshunov, S. Kamba, V. Bovtun, J. Pokorný, M. Savinov, V. Porokhonskyy, D. Rafaja, P. Vaněk, A. Almeida, M. R. Chaves, A. A. Volkov, M. Dressel, and R. Waser, Phys. Rev. B **64**, 184111 (2001).

[14] D. A. Tenne, I. E. Gonenli, A. Soukiassian, D. G. Schlom, S. M. Nakhmanson, K. M. Rabe, and X. X. Xi, Phys. Rev. B **76**, 024303 (2007).

[15] H. Gibhardt, J. Leist, and G. Eckold, Mater. Res. Express **2**, 015005 (2014).

[16] M. Dodge, in *Handbook of Laser Science and Technology, Volume IV, Optical Material: Part 2*, edited by M. J. Webber (CRC Press, Boca Raton, 1986).

[17] D. A. Long, *Raman Spectroscopy* (McGraw-Hill, New York, 1977).

[18] W. Taylor and A. Murray, Solid State Commun. **31**, 937 (1979).

[19] M. I. Aroyo, J. M. Perez-Mato, C. Capillas, E. Kroumova, S. Ivantchev, G. Madariaga, A. Kirov, and H. Wondratschek, Z. Kristallogr. **221**, 15 (2006).

[20] M. I. Aroyo, J. I. Perez-Mato, D. Orobengoa, E. Tasci, G. de la Flor, and A. Kirov, Bulgarian Chem. Commun. **43**, 183 (2011).

[21] E. Kroumova, M. Aroyo, J. Perez-Mato, A. Kirov, C. Capillas, S. Ivantchev, and H. Wondratschek, Phase Transitions **76**, 155 (2003).

[22] M. I. Aroyo, A. Kirov, C. Capillas, J. M. Perez-Mato, and H. Wondratschek, Acta Crystallogr., Sect. A **62**, 115 (2006).

[23] R. Ouillon, J. Pinan-Lucarre, P. Ranson, P. Pruzan, S. K. Mishra, R. Ranjan, and D. Pandey, J. Phys.: Condens. Matter **14**, 2079 (2002).

[24] R. A. Evarestov, E. Blokhin, D. Gryaznov, E. A. Kotomin, and J. Maier, Phys. Rev. B **83**, 134108 (2011).

[25] M. A. Islam, J. M. Rondinelli, and J. E. Spanier, J. Phys.: Condens. Matter **25**, 175902 (2013).

[26] M. A. Geday and A. M. Glazer, J. Phys.: Condens. Matter **16**, 3303 (2004).

[27] R. Schaufele and M. Weber, J. Chem. Phys. **46**, 2859 (1967).

[28] J. Sapriel, Phys. Rev. B **12**, 5128 (1975).

[29] T. A. Merz, H. Noad, R. Xu, H. Inoue, W. Liu, Y. Hikita, A. Vailionis, K. A. Moler, and H. Y. Hwang, Appl. Phys. Lett. **108**, 182901 (2016).

[30] K. A. Müller, W. Berlinger, M. Capizzi, and H. Granicher, Solid State Commun. **8**, 549 (1970).

[31] B. Kalisky, J. A. Bert, C. Bell, Y. Xie, H. K. Sato, M. Hosoda, Y. Hikita, H. Y. Hwang, and K. A. Moler, Nano Lett. **12**, 4055 (2012).

[32] H. Noad, E. M. Spanton, K. C. Nowack, H. Inoue, M. Kim, T. A. Merz, C. Bell, Y. Hikita, R. Xu, W. Liu, A. Vailionis, H. Y. Hwang, and K. A. Moler, Phys. Rev. B **94**, 174516 (2016).